

www.acsami.org Research Article

Biolayer-Interferometry-Guided Functionalization of Screen-Printed Graphene for Label-Free Electrochemical Virus Detection

Beata M. Szydlowska, Cícero C. Pola, Zizhen Cai, Lindsay E. Chaney, Janan Hui, Robert Sheets, Jeremiah Carpenter, Delphine Dean, Jonathan C. Claussen,* Carmen L. Gomes,* and Mark C. Hersam*



Cite This: ACS Appl. Mater. Interfaces 2024, 16, 25169–25180



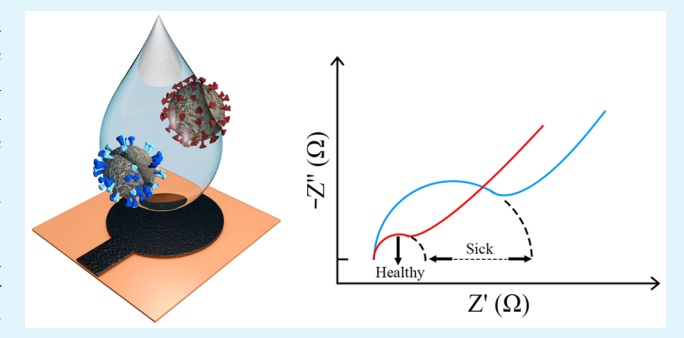
ACCESS I

Metrics & More

Article Recommendations

s Supporting Information

ABSTRACT: Additive manufacturing holds promise for rapid prototyping and low-cost production of biosensors for diverse pathogens. Among additive manufacturing methods, screen printing is particularly desirable for high-throughput production of sensing platforms. However, this technique needs to be combined with carefully formulated inks, rapid postprocessing, and selective functionalization to meet all requirements for high-performance biosensing applications. Here, we present screen-printed graphene electrodes that are processed with thermal annealing to achieve high surface area and electrical conductivity for sensitive biodetection via electrochemical impedance spectroscopy. As a proof-of-concept, this biosensing platform is utilized for



electrochemical detection of SARS-CoV-2. To ensure reliable specificity in the presence of multiple variants, biolayer interferometry (BLI) is used as a label-free and dynamic screening method to identify optimal antibodies for concurrent affinity to the Spike S1 proteins of Delta, Omicron, and Wild Type SARS-CoV-2 variants while maintaining low affinity to competing pathogens such as Influenza H1N1. The BLI-identified antibodies are robustly bound to the graphene electrode surface via oxygen moieties that are introduced during the thermal annealing process. The resulting electrochemical immunosensors achieve superior metrics including rapid detection (55 s readout following 15 min of incubation), low limits of detection (approaching 500 ag/mL for the Omicron variant), and high selectivity toward multiple variants. Importantly, the sensors perform well on clinical saliva samples detecting as few as 10³ copies/mL of SARS-CoV-2 Omicron, following CDC protocols. The combination of the screen-printed graphene sensing platform and effective antibody selection using BLI can be generalized to a wide range of point-of-care immunosensors.

KEYWORDS: electrochemical impedance spectroscopy, biosensing, immunosensor, printed electronics, additive manufacturing

INTRODUCTION

The coronavirus disease, COVID-19, was first reported in December 2019 in Wuhan, China. Because of its high transmissibility, COVID-19 rapidly spread worldwide, resulting in hospitals being overwhelmed with patients experiencing diverse symptoms including dyspnea, fever, chills, cough, bone pain, fatigue, headache, and diarrhea. During the subsequent global pandemic, over 775 million people were infected, and more than 7.0 million deaths were reported by March 2024.² Throughout the COVID-19 pandemic, new variants of SARS-CoV-2 emerged with evolved characteristics such as enhanced symptom severity (Delta variant) or transmission rate (Omicron variant). Despite effective vaccines being available, it is estimated that approximately 30% of the global population has not received even one vaccination dose, especially in lowincome communities with limited access to healthcare.3 Consequently, prompt diagnosis was critical to making informed treatment decisions.4 In particular, diagnostic methods with a low limit of detection (LOD) and broad response to evolving variants are essential to identifying viral

infections at the earliest stages⁵ and gauging the effectiveness of subsequent interventions.⁶

Among COVID-19 diagnostic methods, the reverse transcription—quantitative polymerase chain reaction (RT-qPCR) is the gold standard. While RT-qPCR possesses high accuracy and sensitivity, it also requires detailed analysis by highly skilled personnel in specialized laboratories with high-cost equipment. With soaring demand for tests at the height of the pandemic, rapid antigen-based lateral flow assays (LFAs) became extremely popular, providing an easy-to-use, low-cost, and rapid alternative for point-of-care applications. However, the limited sensitivity and specificity of LFAs undermine its utility as a definitive and conclusive test. Therefore, alternative

Received: March 31, 2024 Revised: April 22, 2024 Accepted: April 23, 2024 Published: May 2, 2024





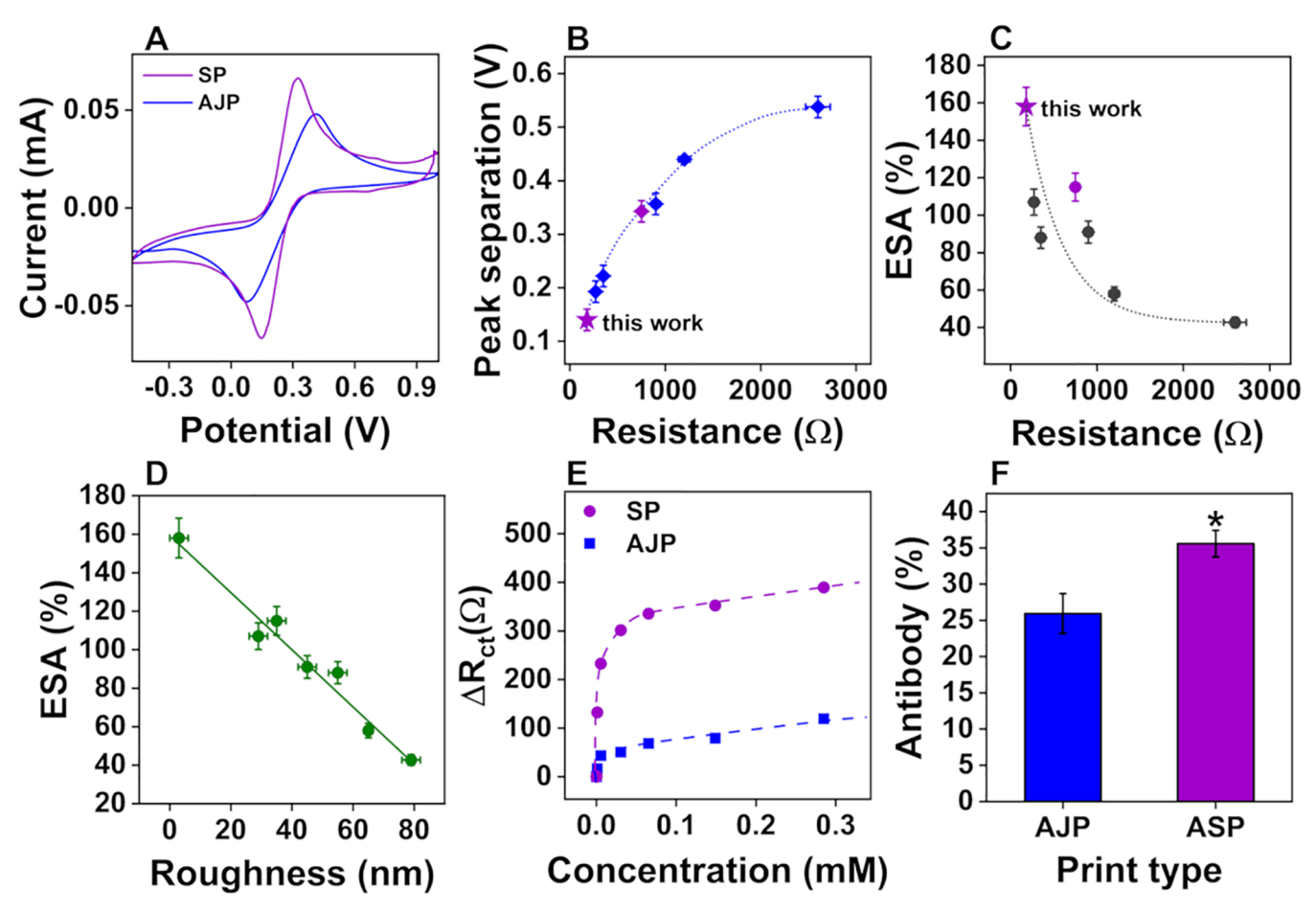


Figure 1. (A) Cyclic voltammograms (CVs) acquired at 25 mV/s from dipstick electrodes printed using screen printing (SP) and aerosol jet printing (AJP). (B) Relationship between the peak separation at 25 mV/s and two-point-probe electrode resistance. The purple star is the optimal SP electrode reported in this work; the purple diamond is the optimal AJP electrode. (B) Relationship between electrochemical surface area (ESA) and two-point-probe electrode resistance. The purple star is the optimal SP electrode reported in this work; the purple diamond is the optimal AJP electrode. ESA was estimated using CVs acquired at various scan rates (5, 15, 25, 50, 100, and 150 mV/s) in the 5 mM Fe(CN)₆³⁻/Fe(CN)₆⁴⁻ redox probe with 0.1 M KCl in 1x PBS. (D) Relationship between ESA and electrode roughness. (E) Comparison between the response of the SP and AJP electrodes to biotin—avidin binding events at different concentrations. (F) Efficiency of the antibody attachment onto the activated surface of SP and AJP electrodes with the Bradford assay. The asterisk (*) indicates a statistically significant (p < 0.05) difference in the amount of attached antibody according to the student t test.

SARS-CoV-2 detection schemes for reliable, rapid, inexpensive, and everyday use have been highly sought. Toward this end, significant effort has been devoted to developing portable nanomaterial-based biosensors^{11,12} that enable accurate diagnosis of infected patients without the need for in-person contact or specialized equipment.

Prominent examples of portable COVID-19 biosensors include graphene-based field-effect-transistor (FET) sensors, colorimetric sensors, multiplexed sensors, and localized surface plasmon resonance (LSPR) sensors as well as electrochemical amperometric and impedance-based sensors. 11-17 Among these cases, electrochemical sensors have attracted significant interest as a result of their high sensitivity, low cost of operation, rapid response, short readout time, and minimal required sample volume.¹⁷ Electrochemical sensors frequently employ electrodes consisting of nanostructured carbon materials, 18,19 such as graphene, graphene oxide, carbon nanotubes, carbon quantum dots, or fullerenes, 12,20,21 due to their large surface-area-to-volume ratios, solution processability that enables rapid additive manufacturing,²² and established functionalization schemes. 23,24 Despite these advantages of carbon nanomaterials, deposition methods strongly influence

film morphology, resulting in challenges with reproducibility. 22,25,26 Common deposition and printing processes include drop-casting, spin-coating, stamping, aerosol jet printing (AJP), inkjet printing, and 3D printing, 22,23,26–30 each of which results in a different film morphology, thickness, roughness, and resolution, all of which can affect electrochemical performance. In contrast, screen printing (SP) offers scalable and low-cost production with the potential for high reproducibility, especially with suitably chosen postprocessing methods. 31,32 In particular, graphene SP electrodes have been widely employed in biosensing platforms for diverse targets including C-reactive proteins for early detection of cardiovascular disease, viral detection even before the COVID-19 pandemic, and broadly understood food safety measures. 33

Screen-printed electrodes are often subjected to surface modification with other materials such as metallic nanoparticles (e.g., copper^{31,32,34} and gold^{31,32,35}), transition metal dichalcogenides (e.g., molybdenum disulfide^{31,32} and tungsten oxide^{31,32}), conductive polymers (e.g., polyaniline^{31,32,36} and polypyrole^{31,32,37}), quantum dots,^{31,32,38} and other carbon-based materials.^{31,32,39} When utilized individually or in combination, these surface modifications result in enhanced

sensitivity and/or more efficient immobilization of the recognition agent, the latter of which is often additionally aided by electrochemical activation. Although these surface modification methods can improve sensor performance, they require additional processing, which elevate production costs and limit manufacturing scalability.

Here, screen-printed graphene electrodes are postprocessed with thermal annealing to achieve high electroactive surface area for sensitive biosensing via electrochemical impedance spectroscopy. Thermal annealing also introduces oxygen moieties on the graphene electrode surface, which enables robust binding to antibody recognition agents. To efficiently identify antibodies with high affinity for target analytes, biolaver interferometry (BLI) is employed. In particular, BLI enables optimal antibodies to be identified for concurrent affinity to the Delta, Omicron, and Wild Type SARS-CoV-2 variants while maintaining low affinity to competing pathogens such as Influenza H1N1. The resulting electrochemical immunosensors achieve superlative metrics including rapid detection and low limits of detection, including for clinical saliva samples following CDC protocols. The generality of the BLI screening method implies that this methodology can be widely applied to diverse biodetection applications.

RESULTS AND DISCUSSION

Screen printing is a high-throughput method of manufacturing predesigned patterns where both ink formulation and substrate choice are crucial to a high-quality print. 22,27 Dipstick electrodes with a previously optimized geometry²³ were screen-printed onto a flexible polyimide substrate (Kapton) with ink formulated from graphene/ethyl cellulose (EC) powder. 42 In particular, the graphene/EC powder was dispersed in terpineol by centrifugal mixing to obtain a uniformly blended slurry (see the Experimental Section for more details).⁴³ The screen-printed patterns are controlled by several process control parameters such as automatic versus manual printing, mesh size, snap-off distance, printing speed, ink concentration, and ink viscosity. 22,25,27,44 Variation of all these parameters individually or in combination results in patterns with the same nominal geometry but considerably different surface morphologies. Examples of these surface morphology differences are presented in the optical micrographs in Figure S1. As a result, the electrical and electrochemical performance of the printed electrode is highly affected.

Since cyclic voltammetry (CV) is a widely used electrochemical technique that rapidly provides information about the performance of electrodes during redox reactions and electron transfer kinetics, 45 CV (Figure 1A) was used to characterize and compare the electrochemical behavior of the screenprinted electrodes developed here with previously reported aerosol-jet-printed electrodes.²³ The characteristic anodic and cathodic CV peaks can be used to extract quantitative information about the electrochemical reversibility of the system, the electron transfer kinetics at the interface between the electrode and electrolyte, and the electroactive surface area (ESA) available for electrochemical reactions.⁴⁶ The value of the two-point-probe resistance (measured between the electrode contact pad and sensing head, Figure S2) varies considerably across prints fabricated with different methods (AJP and SP), ink concentrations (120 and 200 mg/mL), and screen mesh sizes. Hence, two-point probe resistance was used

as a simple but effective quality control measure preceding more rigorous tests of electrochemical performance.

The observed correlation of the two-point-probe resistance with CV peak-to-peak separation (ΔE_{peak}) and ESA (Figure 1B and Figure 1C, respectively) provide a quantitative means for benchmarking different electrodes. Increasing two-point-probe resistance values correlate with an increase in peak-to-peak separation, indicating that low two-point-probe resistance values imply low barrier to electron transfer. 46 The optimized SP-graphene electrodes possess a ΔE_{peak} of 140 \pm 6 mV (Figure 1B, purple star), which is significantly lower than AJPgraphene electrodes⁴² (Figure 1B, purple diamond). Importantly, an electrode with low peak-to-peak separation is desired for electrochemical applications since it indicates a low barrier to electron transfer. Conversely, the ESA calculated from respective CVs at various scan rates (5, 15, 25, 50, 100, and 150 mV/s) rapidly decreased with increasing two-point-probe resistance (Figure 1C). The ESA is also linearly correlated to the print surface roughness (Figure 1D), with the highest effective ESA occurring for the smoothest printed electrodes, indicating a highly electroactive surface. Based on these relationships among ESA, ΔE_{peak} two-point-probe resistance, and surface roughness, electrode performance can be tuned by precisely controlling the print morphology and quickly screened with two-point-probe resistance measurements.

Notably, the aforementioned screening measurements also correlate with sensor responsiveness. This correlation is shown in Figure 1E, where the biotin-avidin complex was used as a model binding system to initially evaluate the electrochemical biosensing performance of the SP electrode compared to previously reported AJP electrodes.²³ Both electrodes were functionalized by drop casting 10 μ L of avidin solution (100 $\mu g/mL$) followed by exposure to the same concentrations of biotin (in the range of 0-0.3 mM). The SP and AJP electrodes were evaluated under the same electrochemical impedance spectroscopy (EIS) conditions. The charge transfer resistance extracted from EIS data is highly sensitive to changes in the interface between the electrode surface and the electrolyte. 47 Consequently, the change in EIS-extracted charge transfer resistance (ΔR_{ct}) is reported in Figure 1E, presenting significantly larger $\Delta R_{\rm ct}(\Omega)$ for SP compared to AJP electrodes. Because both electrodes were exposed to the same concentrations of biotin, the ΔR_{ct} signal can be assumed to be limited primarily by the amount of avidin initially attached to the surface of the electrode. 48 In particular, the smoother surface of the SP compared to the AJP electrodes allows for a more densely packed avidin layer on the SP electrodes. Moreover, the rougher surface of the AJP electrodes leads to an inhomogeneous distribution of electrochemical properties (e.g., electrochemical current density, interfacial capacitance, and solution resistance) across the surface of the electrode, which induces further deviations from an ideal electrochemical response.⁴⁹

Following the initial biotin–avidin assay, we proceeded to functionalize fresh electrodes with the SARS-CoV-2 Spike mouse monoclonal antibody (MM117). Using the Bradford assay (see the Supporting Information for details), ⁵⁰ the concentration of antibodies immobilized on the surface of the electrodes was estimated. The SP electrodes showed significantly more antibody attachment than the AJP electrodes, with $35.59 \pm 1.82\%$ and $25.94 \pm 2.74\%$ immobilization efficiency, respectively (Figure 1F).

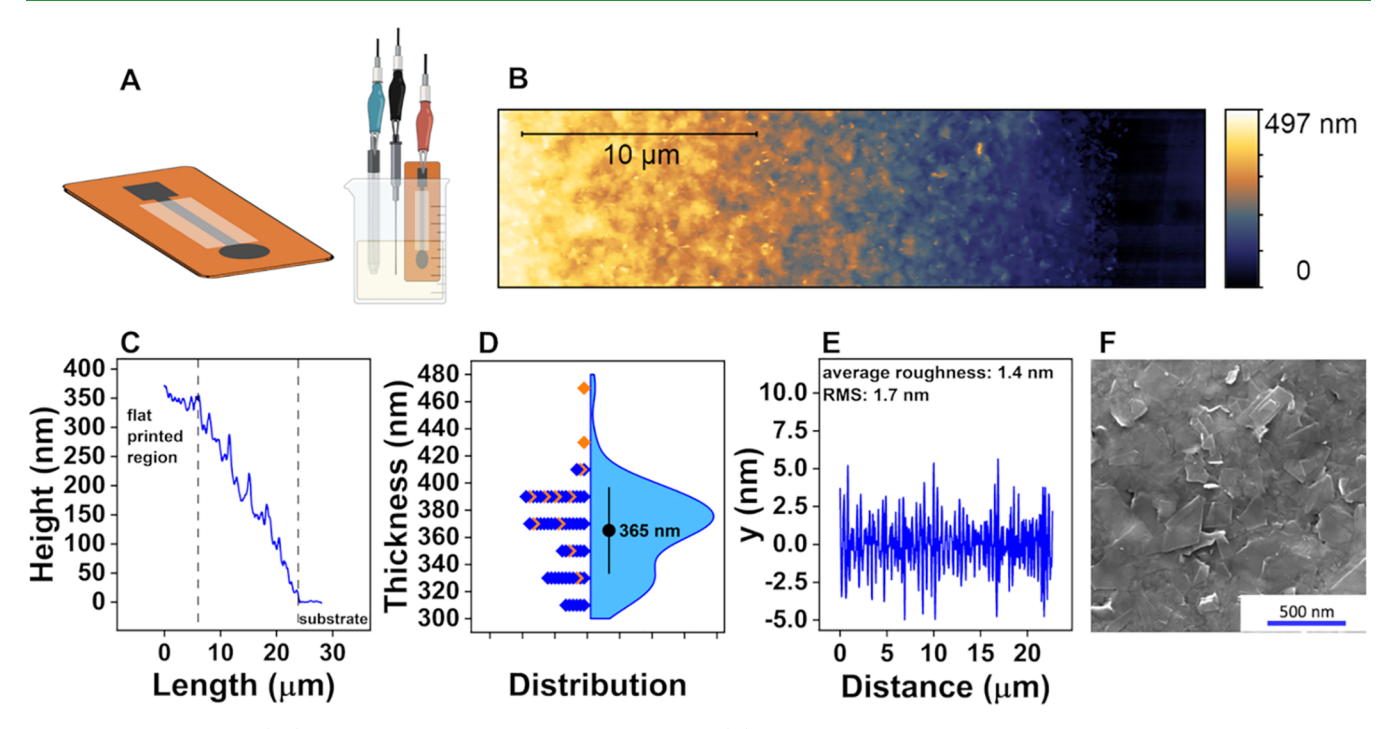


Figure 2. Screen-printed (SP) graphene electrode surface characterization. (A) Schematic of the dipstick electrode and the electrochemical setup. (B) Atomic force microscopy (AFM) image of the electrode surface at the edge of the pattern. (C) Height profile extracted from the AFM image. (D) Print thickness distribution across multiple electrodes measured with AFM (blue) and confocal microscopy (orange). (E) Roughness profile extracted from the AFM image averaged over 100 lines. (F) Scanning electron microscopy (SEM) image of the electrode surface.

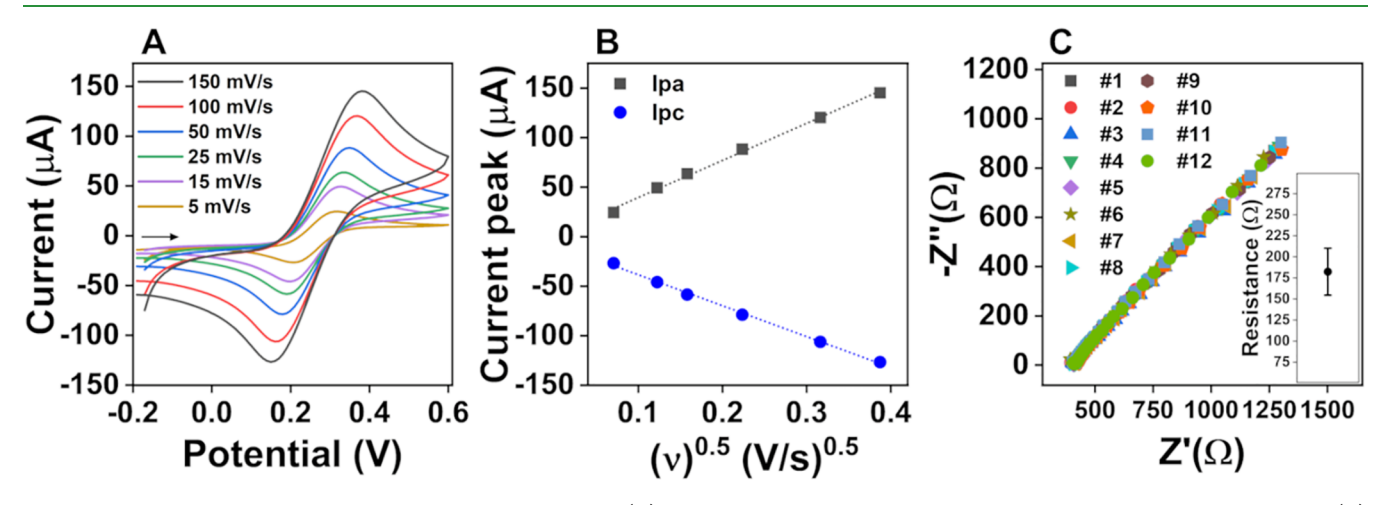


Figure 3. Electrochemical characterization of the SP electrodes. (A) Cyclic voltammograms at 5, 15, 25, 50, 100, and 150 mV/s scan rates. (B) Randles—Sevčik plot showing a linear variation of the peak anodic $(i_{\rm pa})$ and $(i_{\rm pc})$ currents with the square root of the scan rate. All electrochemical measurements were performed in a 5 mM Fe(CN) $_6$ ³⁻/Fe(CN) $_6$ ⁴⁻ redox probe with 0.1 M KCl in 1x PBS. (C) Nyquist plot obtained through electrochemical impedance spectroscopy of bare SP graphene electrodes (n = 12). Inset: as-printed electrode 2-point resistance measured at 25 mm distance.

Considering all of the results presented in Figure 1, the electrode most suitable for SARS-CoV-2 biosensing was defined as presenting a low CV peak-to-peak separation, high ESA, and smooth surface, which should promote high electrochemical reaction kinetics and maximize the output signal generated by changes in the concentration of the target analyte. Following screening of the SP conditions, it was determined that the optimal SP electrodes were produced with SP mesh size, pressure, squeegee snap-off distance, and print speed set to 325 mesh, 20 psi, 1 mm, and 127 mm/s, respectively. Using an automated screen printer, 30 electrodes were produced in each print at a rate equivalent to ~600

electrodes/h when taking into account time for changing substrates and periodically cleaning the SP mesh. Following printing, the electrodes were left to dry (at room temperature) and then thermally annealed at 350 °C for 30 min to remove residual trapped solvent and maximize electrical conductivity. The latter process is governed by the thermal decomposition of the ethyl cellulose binder, which leaves an sp²-rich carbonaceous residue that facilitates charge transport between graphene flakes in the printed percolating network, ultimately leading to a high electrical conductivity of 5×10^4 S/m and low sheet resistance of 43 Ω/sg . Annealing also results in

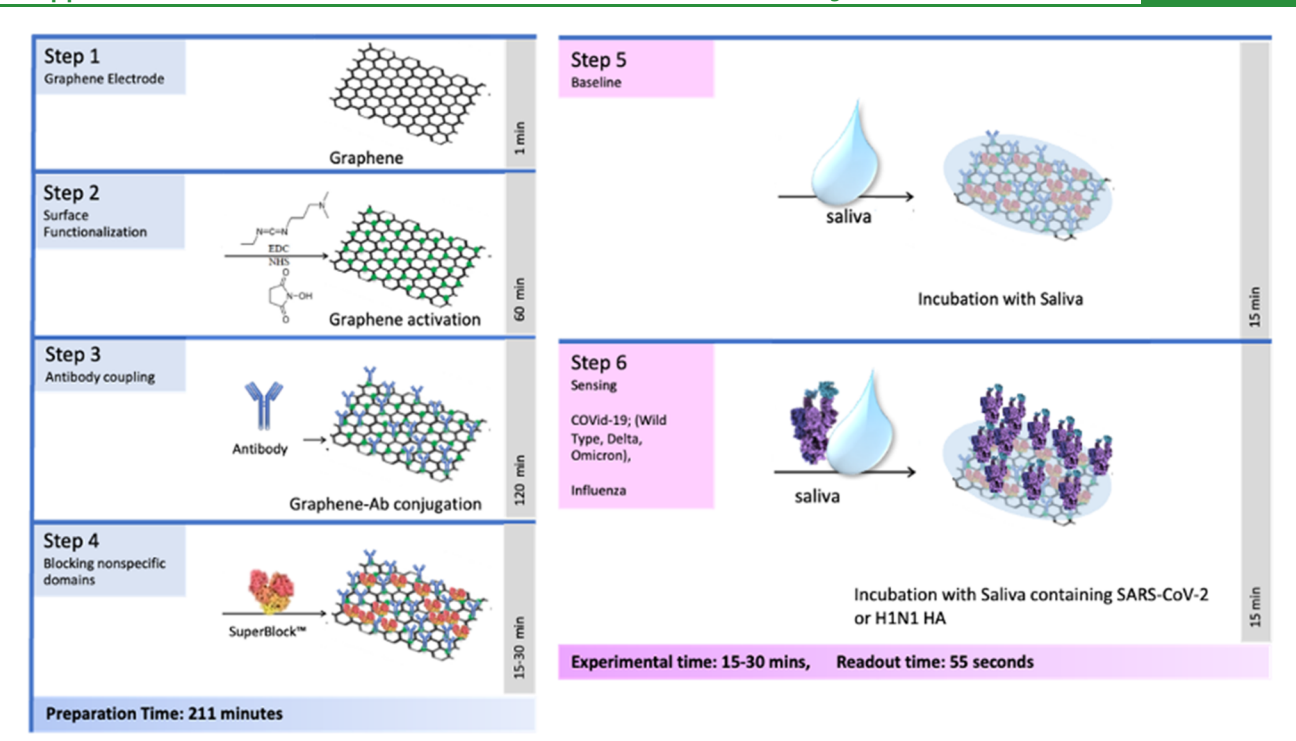


Figure 4. Schematic of the functionalization and sensing protocol. Steps 1–4 constitute the electrode preparation and functionalization. Steps 5 and 6 are for sensing and target detection.

electrodes enriched in oxygenated groups that facilitate functionalization (Figure S3).

The morphology of the SP electrodes was characterized with several microscopic techniques at the region termed the sensing pad working area (Figure 2A). Atomic force microscopy (AFM) (Figure 2B) and profilometry were used to quantify the print thickness and roughness. The height profile marked with the blue dotted line in Figure 2B is provided in Figure 2C, displaying a print thickness of ~350 nm and a surface roughness of ~2 nm. Figure 2D collectively shows thickness measurements performed on 130 randomly chosen electrodes. Blue data points were extracted from AFM, while orange data points were extracted from profilometry. These two complementary measurements corroborated the initial AFM thickness estimate with an average print thickness of 365 nm. Detailed analysis of the AFM spectral profiles performed with Gwyddion similarly corroborated the initial AFM roughness estimate with an average roughness of 1.7 nm (measured across 5 μ m). A representative roughness profile is provided in Figure 2E. Additionally, scanning electron microscopy (SEM) was performed to gain further insight into the surface morphology of the SP graphene patterns (Figure 2F), revealing a flat, well-packed, and aligned graphene flake structure with the graphene nanosheet basal planes lying flat at the electrode surface, which is ideal for efficient electron transfer throughout the SP electrode. 51,52

The electrochemical performance of the SP graphene electrodes was evaluated by CV. Preceding electrochemical measurements, the working area (Figure 2A) was defined by applying a thin layer of fast-drying polymeric lacquer on the shank of the electrode (Figure S4). Subsequent CV measurements (Figure 3A) showed characteristic redox peaks at all applied scan rates (5, 15, 25, 50, 100, and 150 mV/s) between 149.80 and 379.65 mV. The anodic (i_{pa}) and cathodic peak (i_{pc}) currents scaled linearly with the square root of the

respective scan rate (Figure 3B), indicating a diffusion-controlled system. 53,54 Increasing the scan rate resulted in higher peak-to-peak separation ($\Delta E_{\rm peak}$) from 109.92 to 229.84 mV. This change suggests a limitation in electron transfer kinetics^{55,56} and points toward a quasi-reversible electrochemical system controlled by charge transfer and mass transport. 53,55,57 The estimated heterogeneous charge transfer rate constant (k^0) was $9.43 \times 10^{-4} \pm 3.03 \times 10^{-5}$ cm/s, lying within a range between short-time-achieved equilibrium (above 10⁻¹ cm/s) and a sluggish system (below 10⁻⁵ cm/ s). The k^0 value further suggests a system where the current flow is controlled by both charge transfer and mass transport.⁵⁷ Therefore, the ESA of the SP graphene electrodes was extracted from the acquired CV curves using the Randles-Sevčik equation for quasi-reversible systems (see the Supporting Information for details). The ESA of the SP graphene electrodes was $11.23 \pm 0.28 \text{ mm}^2$, corresponding to $158.93 \pm 3.91\%$ of the electrode geometric surface area (7.07) mm²). The defects present in the graphene basal and edge sites, which are apparent in Raman spectroscopy measurements (Figure S3), provide a surface rich in electroactive sites for redox reactions.

Further electrochemical characterization of the SP electrodes was performed using EIS. During EIS, a DC potential is applied relative to the reference electrode along with an additional small sinusoidal AC component of fixed amplitude, 53,54 allowing the frequency dependence of the impedance to be obtained. Normally, EIS data are plotted on a complex plane where the negative of the imaginary impedance is plotted versus the real impedance. The charge transfer resistance ($R_{\rm ct}$) is equivalent to the diameter of the semicircle observed in the EIS complex plane diagram. Examples of the EIS responses for randomly chosen SP electrodes (n = 12) are provided in Figure 3C. Each case consists of a hardly noticeable semicircular region and a diagonal line indicating a facile

electron transfer that is consistent with a mass transfer predominant system. 56 Importantly, the virtually identical signal shape from each sensor confirms the high electrochemical reproducibility of the platform.

Figure 4 outlines the four functionalization steps followed by two sensing steps utilized in our electrochemical biosensing procedure. While full details are provided in the Experimental Section, a brief description of the four functionalization steps is provided here: (1) Graphene electrodes are fabricated by screen printing and thermally processed, resulting in oxygencontaining moieties on the surface. (2) The graphene surface is activated with an EDC:NHS mixture. (3) Antibody coupling is achieved by introducing PBS-based antibodies onto the wet, preactivated surface. (4) Nonspecific binding is blocked with Superblock. Importantly, the antibody-spike couple with the highest binding affinity was identified prior to the third functionalization step with BLI (full BLI details provided in the Supporting Information). Specifically, the interaction between the antibody and the spike protein can be described by the K_D constant, where the antibody MM117 was determined to have high affinity toward SARS-CoV-2 Wild Type (S1), Delta (S1), and Omicron (S1) while simultaneously showing low affinity toward Influenza H1N1 HA (Table 1).

Table 1. $K_{\rm D}$ Values Obtained via Biolayer Interferometry (BLI) for Interaction between the MM117 Antibody and the Spike Protein for Various SARS-CoV-2 Variants in Addition to Influenza H1N1

	target			
	Wild Type	Delta	Omicron	Influenza
antibody	(S1)	(S1)	(S1)	(H1N1)
MM117	1.28×10^{-7}	1.48×10^{-7}	3.96×10^{-8}	1.45×10^{-3}

Following functionalization, the SP electrodes were tested for sensing SARS-CoV-2 Spike S1 protein in an artificial saliva solution. The sensing process has two steps: baseline measurement and detection (Figure 4, Step 5 and Step 6, respectively). For the baseline measurement, the functionalized electrodes were incubated with 5 μ L of artificial saliva for 15 min and rinsed gently with 1x PBS. At this stage, the platform is fully prepared and ready to use for biosensing. Subsequently, the electrode was incubated for 15 min with SARS-CoV-2 Spike S1 protein, rinsed with 1x PBS, and followed by EIS readout (55 s). Each electrode was subjected to the aforementioned functionalization and sensing steps. As additional components were immobilized or bonded to the electrode surface in each step, an insulating effect was produced as shown in Figure 5A, where the electrode surface activation, antibody immobilization, surface blocking, and initial incubation in saliva increased the R_{ct} compared to the bare SP electrode. 55,56 Later, changes to the electrode surface were quantitatively monitored through EIS $R_{\rm ct}$ readout to determine biosensor performance.

Since the initial incubation in the artificial saliva sample increased the electrode $R_{\rm ct}$ (Figure 5A), evaluating the biosensor stability in this medium was crucial to eliminate its contribution and thus avoid false positive results. For this test, a baseline calibration was performed to investigate any changes promoted by the subsequent incubation of artificial saliva solution at the surface of the electrode. In particular, the SP electrodes were initially incubated with artificial saliva solution

for 15 min followed by EIS measurement (Figure 5A). The same SP electrodes were then incubated for another 15 min with artificial saliva solution, after which the EIS was again recorded (Figure 5A). Minimal $R_{\rm ct}$ signal change (3.52 \pm 1.84%, n=20; Figure S5) is observed in the second 15 min incubation, which confirmed that the initial 15 min incubation is sufficient to establish the baseline.

The SARS-CoV-2 sensing performance was assessed by incubating the biosensors with SARS-CoV-2 Spike S1 Omicron (Spike S1 Omicron) in the range of 10 fg/mL to 10 μ g/mL (130.75 aM to 130.75 nM) in artificial saliva. Representative EIS responses to various Spike S1 Omicron concentrations are presented in Figure 5B. The contribution of the semicircular region increases with increased Spike S1 Omicron concentration, directly reflecting changes in R_{ct} , which corresponds to the Spike S1 Omicron bonding to the surface-immobilized antibodies. To determine the selectivity of the biosensors, Influenza A H1N1 hemagglutinin (H1N1 HA) was tested as a potential interferent. The biosensors presented minimal cross-reactivity with the Influenza A H1N1 HA protein with an average $\Delta R_{\rm ct}$ of only 7.21% across 10 orders of magnitude (10 fg/mL to 10 μ g/mL) concentration range (Figure 5C). The change in the signal recorded with EIS (ΔR_{ct}) plotted versus the concentration of different Spike S1 variants was used to construct a biosensor calibration curve (Figure 5D) and evaluate the overall biosensor performance. The biosensor operates in a linear range from 10 fg/mL to 10 μ g/mL ($R^2_{\text{adj}} = 99.07\%$, $p_{\text{model}} < 0.001$, $p_{\text{lack-of-fit}} = 0.193$), with a sensitivity of 10.38 \pm 0.63 ΔR_{ct} (%)/log(fg/mL) and an exceptionally low limit of detection (LOD) equal to 524.67 ± 31.76 ag/mL for Spike S1 Omicron (Figure 5E).

The biosensor was further tested against SARS-CoV-2 Spike S1 Wild Type (Spike S1-WT) and Delta variants (Spike S1 Delta) to show its versatility. In both cases, the biosensors exhibited linear sensing range and competitive sensitivity. Specifically, for Spike S1-WT, linear sensitivity occurs in the range from 1 pg/mL to 1 μ g/mL (R^2_{adj} = 98.93%, p_{model} < 0.001, $p_{\text{lack-of-fit}} = 0.343$), with a sensitivity of 10.51 \pm 0.74 ΔR_{ct} $(\%)/\log(fg/mL)$ and LOD of 486.26 \pm 34.28 fg/mL. Meanwhile, for Spike S1-Delta, linear sensitivity occurs in the range from 1 pg/mL to 10 μ g/mL ($R^2_{adj} = 97.68\%$, $p_{model} <$ 0.001, $p_{\text{lack-of-fit}} = 0.194$), with a sensitivity of 13.63 \pm 1.08 ΔR_{ct} $(\%)/\log(fg/mL)$ and LOD of 170.91 \pm 13.50 fg/mL. These results are highly competitive compared to the literature precedent, especially when considering that these biosensors do not require complicated electrochemical activation, surface modification, or mediators commonly used to aid sensing performance (Table S1). Most notably, the LOD for SARS-CoV-2 Spike S1 Omicron (524.67 \pm 31.76 ag/mL) is unprecedented in the field and showcases how the optimized SP electrodes and BLI-guided antibody choice can lead to exceptionally high biosensing performance.

To further illustrate the advantages of our approach, it is worthwhile to benchmark other SP electrochemical sensing devices that have been reported in the literature. For example, Torres et al. reported an enzymatic biosensor (ACE2-functionalized) that detected SARS-CoV-2 Spike protein with a broad sensing range in saliva samples in only 4 min. S8 Despite the impressive response time, this device only achieved a LOD of 1.39 pg/mL, which is orders of magnitude higher than our SP biosensor. Sample preconcentration using magnetic beads is also a strategy reported in the literature in combination with commercial or in-house fabricated SP

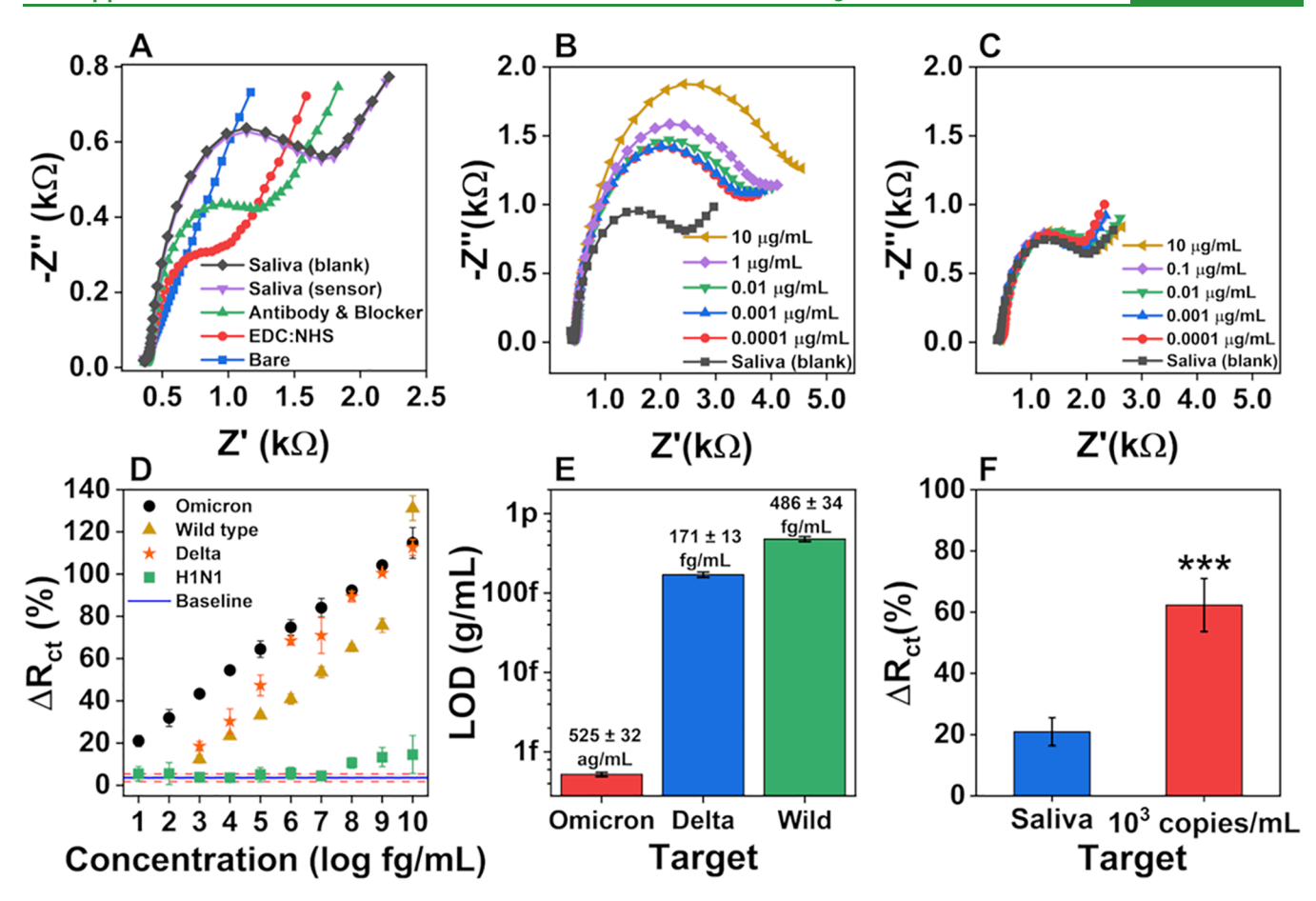


Figure 5. Biosensing characterization. (A) Nyquist plot recorded via EIS at each step of the functionalization protocol. (B) Nyquist plots recorded via EIS that demonstrate the sensor response to various SARS-CoV-2 Spike S1 Omicron concentrations. (C) Nyquist plots recorded via EIS demonstrate the lack of sensor response to various concentrations of Influenza H1N1. (D) Calibration plot showing the percentage change of the signal readout (charge transfer resistance) for the baseline (10% artificial saliva in 1x PBS) and in the presence of SARS-CoV-2 Spike S1 protein for three variants: Omicron, Delta, and Wild Type at concentrations between 10 fg/mL and 10 μ g/mL in addition to various concentrations of Influenza H1N1. (E) Bar plot showing the limit of detection for Omicron, Delta, and Wild Type variants of SARS-CoV-2. (F) Positive SARS-CoV-2 clinical sample biosensing: relative charge transfer resistance percentage for SARS-CoV-2 negative pooled saliva (10% v/v in 1x PBS) and SARS-CoV-2 positive samples at 10³ copies/mL. Error bars represent the standard deviation calculated from 6 independently functionalized electrodes (n = 6). ***A significant (p < 0.0001) increase in ΔR_{ct} (%) according to the Student t test.

electrodes. Even with the use of preconcentration, the devices reported by Malla et al.⁵⁹ and Fabiani et al.⁶⁰ required incubation for 30 min and resulted in significantly higher LODs (0.2 ng/mL and 19 ng/mL, respectively) than our SP biosensor. Modifying electrodes with nanostructures is another common approach to increase the electrochemical sensing performance of SP electrodes. In particular, Mehmandoust et al. developed an enzymatic label-free biosensor for the electrochemical detection of the SARS-CoV-2 Spike protein consisting of a commercial SP electrode modified with silicon oxide nanoparticles in a zirconium(IV) carboxylated metalorganic framework to increase the electron transfer on the electrode surface. 61 Despite the involved nanostructure functionalization scheme, this device only achieved a LOD of 100 fg/mL and a linear sensing range from 100 fg/mL to 10 ng/mL with a response time of 30 min. Another case reported by Fortunati et al.⁶² used SP carbon nanotube electrodes decorated with gold nanoparticles, which only resulted in a narrow linear sensing range (0.5-5 μ g/mL) and high LOD (12 ng/mL). Finally, Hussein et al. used carbon nanotubes and WO₃ to modify a SP electrode to achieve a short response time

of 5 min for SARS-CoV-2 virus particles, but the LOD was 5 orders of magnitude higher than our SP biosensors. ⁶³

As the ultimate test of our SP biosensors, we evaluated them against SARS-CoV-2 clinical samples obtained from deidentified positive patients. The concentration of SARS-CoV-2 in the clinical samples was quantified using qRT-PCR and adjusted to 10³ copies/mL using the negative pooled saliva samples (10% v/v in 1x PBS). In this case, the SP graphene electrodes were prepared and functionalized in the same manner as previously described. Then, a blank sample, consisting of a negative SARS-CoV-2 pooled saliva sample (10% v/v in sterile 1x PBS buffer), was used for baseline measurement and evaluation of ΔR_{ct} (%) for a SARS-CoV-2-free sample, yielding an EIS signal change (ΔR_{ct}) of 20.95 \pm 4.56% (Figure S5A,B). The higher baseline signal variation compared to the artificial saliva samples $(3.52 \pm 1.84\%)$ can be attributed to the more complex composition of the pooled patient saliva. Nevertheless, as shown in Figure 5F, incubation for 30 min with positive saliva samples containing 10³ copies/mL of active SARS-CoV-2 Omicron led to a ΔR_{ct} of 65.34 \pm 8.65%, which is significantly (p < 0.0001) larger than the change induced by the negative saliva sample. Therefore, our SP biosensors were able to

definitively differentiate SARS-CoV-2 Omicron negative from positive (10^3 copies/mL) saliva samples, which complies with CDC requirements for diagnostic or confirmation purposes. Notably, the SP graphene biosensor performs considerably better than commonly available lateral flow assay (LFA) antigen-based rapid tests. In addition to unpleasant nasal swab sampling, most LFA devices require 10^5 to 10^6 copies/mL to differentiate positive from negative samples consistently. $^{58,65-68}$

CONCLUSIONS

Carefully tailored graphene ink formulation coupled with multifactor-controlled screen printing has been used for the high-throughput fabrication of reliable graphene electrochemical sensing electrodes with exceptional batch-to-batch reproducibility. Tuning the fabrication process conditions yielded prints with desirable surface morphology that directly influenced the electrical and electrochemical performance of the final biosensor. Thermal annealing following screen printing introduced additional oxygenated groups favorable for carbodiimide immobilization of antibodies. The final biosensor exhibited superior responsiveness and selectivity to multiple SARS-CoV-2 Spike S1 protein variants including an exceptionally low LOD (524.67 ag/mL) in artificial saliva operating in a broad linear range of 10 fg/mL to 10 μ g/mL for SARS-CoV-2 Spike S1 Omicron. This biosensor can also successfully detect SARS-CoV-2 Wild Type and Delta variants with competitive LODs of 486.26 and 170.91 fg/mL, respectively. Notably, minimal response to the potential interferent Influenza A H1N1 HA confirms the high selectivity that is required for definitive detection of SARS-CoV-2 compared to other common pathogens. Importantly, the SP graphene biosensor was shown to be effective on clinical samples at a level that complies with CDC requirements for diagnostic purposes. 64,69 The optimized SP graphene electrodes can be directly combined with screen-printed Ag/AgCl reference and counter electrodes, thus enabling highthroughput fabrication of an all-in-one sensing platform that can be customized for not only pathogen detection but also other targets of interest in health, agricultural, and environmental applications.

■ EXPERIMENTAL SECTION

Materials. Graphite flakes, ethyl cellulose $(4 \times 10^{-3} \text{ Pa/s})$, terpineol, N-(3-(dimethylamino)propyl)-N'-ethylcarbodiimide (EDC), N-hydroxysuccinimide (NHS), 2-(N-morpholino)ethanesulfonic acid (MES buffer), potassium hexacyanoferrate(II) trihydrate, and potassium ferricyanide were purchased from MilliporeSigma (St. Louis, MO). Potassium chloride was purchased from Fisher Scientific (Hampton, NH). Superblock blocking buffer and 200-proof ethanol were purchased from Thermo Fisher (Waltham, MA). Artificial saliva was purchased from Pickering Laboratories (Mountain View, CA). Phosphate buffer saline was purchased from Alfa Aesar (Tewksbury, MA). SARS-CoV-2 Spike mouse monoclonal antibody, SARS-CoV-2 B.1.1.529 Omicron variant Spike S1 protein, SARS-CoV-2 B.1.617.2 Delta variant Spike S1 protein, SARS-CoV-2 Wild-Type Spike S1 protein, and Influenza A H1N1 hemagglutinin protein were purchased from Sino Biological (Sino Biological US Inc., Wayne, PA).

Graphene Exfoliation. Graphene powder was prepared according to a previously reported procedure. Briefly, graphite flakes, ethyl cellulose (EC), and ~20 L of ethanol were mixed in a weight ratio of 30:1:20 and processed for 24 h in a Silverson 200 L high-shear in-line mixer at maximum power. The slurry was centrifuged, flocculated, washed, and dried to obtain a powder of exfoliated graphene

nanosheets stabilized with EC. This procedure yields a standard batch of 40-50 g of graphene/EC powder containing $\sim\!40$ wt % graphene for redispersion in organic solvents.

Graphene Ink Formulation. The graphene/EC powder was dispersed in terpineol via centrifugal mixing (ARE-310, Thinky USA) using ceramic ball bearings in a four-step process that was repeated twice: (1) 3 min, 800 rpm; (2) 3 min, 12000 rpm; (3) 3 min, 1600 rpm; (4) 3 min, 2000 rpm. Ink concentrations of 100–200 mg/mL were compatible with screen printing, and an ideal concentration of 140 mg/mL was chosen to optimize print resolution and minimize screen cleaning. About 3 mL of ink was prepared at a time.

Screen Printing. The electrodes were printed using an automated screen printer (886PC DSIV, Hary Manufacturing Inc.) using mesh size, squeegee pressure, squeegee snap-off distance, and print speed set to 325 mesh, 20 psi, 1 mm, and 127 mm/s, respectively. About 30 electrodes were produced in one print, and an estimated 600 electrodes could be produced per hour, considering the substrate change time and periodic mesh cleaning time. As-printed patterns were dried in air and then thermally cured at 350 °C for 30 min.

Atomic Force Microscopy. To obtain topographic characterization of the printed graphene films, atomic force microscopy (AFM) was performed using an Asylum Cypher AFM (Oxford Instruments, Abingdon, UK). Individual graphene nanosheets and graphene prints were characterized with the Cypher AFM in tapping mode using Si cantilevers with a resonance frequency of ~320 kHz. Scanning parameters were fixed at 1024 pixels/line and a 0.8 Hz scan rate. AFM scans were graphically processed with the use of Gwyddion software equipped with tools such as scar removal, denoising, and background flattening. The height profile and surface statistical analysis tools of Gwyddion were also used to evaluate the roughness and thickness of the printed graphene electrodes.

Profilometry. Profilometry (Veeco, Dektak 150) was used to evaluate the thickness and roughness of the printed graphene structures.

Scanning Electron Microscopy. Scanning electron microscopy (SEM) images of the SP graphene electrodes were obtained using an FEI Quanta 250 FE-SEM (Thermo Fisher Scientific, Portland, OR). Samples were coated with a 2 nm layer of iridium using a turbo pump sputter coater (Quorum Technologies, East Sussex, UK) to reduce charging effects. Images were acquired using an accelerating voltage of 10 kV, a spot size 3.0, and a working distance of 10 nm.

Raman Spectroscopy. Raman spectra were obtained using a Horiba XploRa PLUS microscope (Horiba, Kyoto, Japan) with a 532 nm laser and 1800 mm⁻¹ grating. Each spectrum was obtained with 10% laser power and averaged over 5 acquisitions, each with a duration of 10 s.

Confocal Microscopy. An Olympus 3D laser confocal microscope was also used to evaluate print thickness and surface roughness. Images of 50 μ m \times 50 μ m in size were taken in 3D mapping mode and later postprocessed with ImageJ software to extract the thickness and roughness values.

X-ray Photoelectron Spectroscopy. Graphene films were characterized after thermal curing using X-ray photoelectron spectroscopy (XPS) performed on a Thermo Scientific ESCALAB 250Xi (Thermo Fisher Scientific, Waltham, MA) equipped with an Al $K\alpha$ radiation source. Spectra for the C 1s peak (279.2–298.2 eV with a step size of 0.1 eV) was obtained in at least three spots per sample with a spot size of 500 μ m. Each XPS spectrum was fit in the Thermo Avantage software using the Knowledge Base graphene data as a guiding reference. Several fit variations were tested before concluding that the C 1s spectrum was the best fit, with only two peaks representing the asymmetric C–C sp² and C=O signals.

Electrochemical Measurements. SP electrodes were electrochemically characterized through cyclic voltammetry (CV) and electrochemical impedance spectroscopy (EIS) using both a PalmSens4 potentiostat (PalmSens, Utrecht, Netherlands) and a BioLogic workstation (BioLogic, Sevssinet-Pariset, France). All electrochemical measurements were performed in 5 mM Fe-(CN)₆³⁻/Fe(CN)₆⁴⁻ (ferri-/ferrocyanide) redox probe with 0.1 M KCl in 1x PBS using a three-electrode setup with an Ag/AgCl

reference electrode and a Pt-wire counter electrode. CV measurements were performed in a sweep range from -0.4 to 0.6 V with scan rates of 5, 10, 25, 50, 100, and 150 mV/s. EIS measurements were performed using a frequency range from 0.1 Hz to 10 kHz with an AC potential amplitude of 10 mV and a DC bias of 0.25 V. Complex plane diagrams were fitted to determine the charge transfer resistance ($R_{\rm ct}$), the series resistance ($R_{\rm s}$), the double-layer capacitance ($C_{\rm dl}$), and the Warburg impedance ($Z_{\rm W}$) by fitting the data set to the Randles–Ershler circuit model using the PSTrace v.5.8 (PalmSens) and the EC-Lab v.11.36 (BioLogic) software.

SP Electrode Functionalization. The isolated working area of the SP graphene electrode was functionalized in a multistep process: (1) The graphene electrode is screen printed and annealed as delineated above. (2) The graphene surface was activated with 5 μ L of a 4:1 EDC:NHS mixture (prepared in 0.1 M MES buffer pH 6.0) and incubated for 60 min under vertical agitation at room temperature. (3) Antibody coupling was achieved by introducing 5 μ L of the 50 μ g/mL PBS-based antibody solution onto the wet, preactivated surface for 120 min under horizontal agitation at room temperature and in a humid environment (to prevent evaporation). (4) Nonspecific binding was blocked using 4 μ L of Superblock:PBS (1:1 mixture) for 15 min followed by rinsing with 1xPBS as in the previous steps.

SARS-CoV-2 Spike S1 Sensing. Standard solutions containing SARS-CoV-2 Spike S1 Omicron, Wild Type, and Delta variants were prepared in artificial saliva with 1x PBS (1:1) in concentrations ranging from 10 fg/mL to 10 μ g/mL (130.75 aM to 130.75 nM). SP graphene electrodes were incubated with 5 μ L of a 1x PBS solution containing different concentrations of SARS-CoV-2 Spike S1 for 15 min to allow the interaction between the SARS-CoV-2 Spike S1 protein and the antibody immobilized on the surface of the electrode. The electrodes were washed with 100 μ L of 1x PBS between each measurement to remove the residual ferro-/ferricyanide. The baseline of the SP biosensors was acquired by evaluating the change in R_{ct} promoted by two subsequential incubations in an artificial saliva solution without any Spike S1 protein. SARS-CoV-2 Spike S1 calibration plots were obtained by measuring the change in the charge transfer resistance (R_{ct}) for each concentration tested in relation to the baseline. Considering the possible presence of interferent molecules in a saliva sample, selectivity was evaluated against Influenza A H1N1 HA. The SP biosensors were incubated with concentrations of H1N1, ranging from 10 fg/mL to 10 μ g/mL, in artificial saliva solution under the same conditions as the SARS-CoV-2 sensing experiments, and the change in Rct during EIS measurements was evaluated.

Clinical Samples. The studies involving human participants were reviewed and approved by the Clemson University Institutional Review Board (IRB) (approval numbers: IRB2021-0703 and IRB2021-0445). The participants provided their written informed consent to participate in this study. Saliva samples were collected following established protocols⁷⁰ from patients at Clemson University and community COVID-19 testing centers (Clemson, SC),⁷¹ who were undergoing diagnostic testing during January 2022. Samples were stripped of personal identifiers, and one aliquot was used to quantify the viral load of SARS-CoV-2 at the Clemson University Research and Education in Disease Diagnosis and Intervention (REDDI) Lab (CLIA# 42D2193465). The TigerSaliva multiplex RTqPCR saliva diagnosis test was used to quantify the concentration of the SARS-CoV-2 virus in the clinical samples using previously established methods.^{72–74} Briefly, the saliva samples were heat-treated at 95 °C for 30 min, and 2 μ L was transferred automatically to a 384well plate by an open-source sample handler (Opentrons OT-2). The plates were loaded into a thermocycler (Bio-Rad CFX 384) for amplification. During this test, the N1 sequence of SARS-CoV-2 was measured (primers: Integrated DNA Technologies (IDT) 1006830 nCoV_N1 forward primer, reverse primer IDT 10006831, probe IDT 10006832; human control gene: Hs RPP30; RNA P forward primer: IDT 10006836, reverse primer 10006837, probe IDT 10007062, RNase P (ATTO 647) probe). Considering that the N-gene is a single-copy gene, the number of N-gene is equivalent to the number

of virus copies, and the results are reported as copies of the virus per sample volume. The performance of the SP graphene biosensors was also evaluated against SARS-CoV-2 clinical samples obtained from deidentified positive patients. SARS-CoV-2 negative pooled saliva samples (10% v/v in sterile 1x PBS buffer) were used as blank samples for baseline measurement. A sample aliquot of 15 μ L was drop-casted on the working area of the SP graphene biosensor and incubated for 30 min before EIS measurements. The percentage $\Delta R_{\rm ct}$ obtained after two consecutive incubations with SARS-CoV-2 negative pooled saliva samples was used as the biosensor baseline. Similarly, the SP graphene biosensor was tested with SARS-CoV-2 positive saliva samples containing 10^3 copies/mL. The percentage $\Delta R_{\rm ct}$ promoted by the positive SARS-CoV-2 clinical samples was reported in relation to the negative pooled saliva sample (blank).

Statistical Analysis. A completely randomized design was used in this study with at least three replicates, and the results were reported as mean \pm standard deviation. Data analysis was performed using JMP Pro statistical software (version 16, SAS, Cary, NC). Differences between variables were tested using the student t test at a level of significance of 5% (α = 0.05). Regression analysis with a confidence level of 95% was performed to determine the linear sensing range and the functional correspondence among quantitative variables. Limits of detection (LOD) for the biosensors were calculated using the 3σ method. The sum of the student 3σ method.

ASSOCIATED CONTENT

Supporting Information

The Supporting Information is available free of charge at https://pubs.acs.org/doi/10.1021/acsami.4c05264.

Print morphology; heterogeneous electron transfer rate (k^0) and electroactive surface area (ESA) methods; two-point probe resistance measurement; quantification of immobilized antibody; Raman and X-ray photoelectron spectroscopy results; active surface delineation; biolayer interferometry (BLI) methodology; baseline reproducibility; biosensing of clinical samples; benchmarking table (PDF)

AUTHOR INFORMATION

Corresponding Authors

Mark C. Hersam — Department of Materials Science and Engineering, Northwestern University, Evanston, Illinois 60208, United States; Department of Chemistry and Department of Electrical and Computer Engineering, Northwestern University, Evanston, Illinois 60208, United States; orcid.org/0000-0003-4120-1426; Email: m-hersam@northwestern.edu

Carmen L. Gomes — Department of Mechanical Engineering, Iowa State University, Ames, Iowa 50011, United States; orcid.org/0000-0003-0095-6478; Email: carmen@iastate.edu

Jonathan C. Claussen – Department of Mechanical Engineering, Iowa State University, Ames, Iowa 50011, United States; o orcid.org/0000-0001-7065-1077; Email: jcclauss@iastate.edu

Authors

Beata M. Szydlowska — Department of Materials Science and Engineering, Northwestern University, Evanston, Illinois 60208, United States

Cícero C. Pola — Department of Mechanical Engineering, Iowa State University, Ames, Iowa 50011, United States; orcid.org/0000-0001-6141-9698

- Zizhen Cai Department of Materials Science and Engineering, Northwestern University, Evanston, Illinois 60208, United States
- Lindsay E. Chaney Department of Materials Science and Engineering, Northwestern University, Evanston, Illinois 60208, United States
- Janan Hui Department of Chemistry, Northwestern University, Evanston, Illinois 60208, United States
- Robert Sheets Department of Mechanical Engineering, Iowa State University, Ames, Iowa 50011, United States
- Jeremiah Carpenter Center for Innovative Medical Devices and Sensors (REDDI Lab), Clemson University, Clemson, South Carolina 29634, United States; Department of Bioengineering, Clemson University, Clemson, South Carolina 29634, United States
- Delphine Dean Center for Innovative Medical Devices and Sensors (REDDI Lab), Clemson University, Clemson, South Carolina 29634, United States; Department of Bioengineering, Clemson University, Clemson, South Carolina 29634, United States

Complete contact information is available at: https://pubs.acs.org/10.1021/acsami.4c05264

Author Contributions

B.M.S. and C.C.P. contributed equally to this work.

Notes

The authors declare no competing financial interest.

ACKNOWLEDGMENTS

The authors gratefully acknowledge funding support for this work from the Centers for Disease Control and Prevention under contract numbers 75D30121C10238 and U01AA029328 in addition to the National Institutes of Health under grant number U01 AA029328/AA/NIAAA NIH HHS/United States. Graphene powder production was supported by National Science Foundation Future Manufacturing Program (NSF CMMI-2037026). Screen printing was supported by the U.S. Department of Commerce, National Institute of Standards and Technology (Award 70NANB19H005) as part of the Center for Hierarchical Materials Design (CHiMaD). B.M.S. also thanks Deutsche Forschungsgemeinschaft (DFG) for funds within the framework of the Benjamin Walter Fellowship (agreement SZ 463/1-1). Figures 2 and 4 were created with BioRender.com.

REFERENCES

- (1) de Wit, E.; van Doremalen, N.; Falzarano, D.; Munster, V. J. SARS and MERS: recent insights into emerging coronaviruses. *Nat. Rev. Microbiol.* **2016**, *14*, 523–534.
- (2) WHO Coronavirus (COVID-19) Dashboard, 2023. https://covid19.who.int/ (accessed 2022-10-03).
- (3) WHO Coronavirus (COVID-19) Dashboard Vaccination, 2023. https://covid19.who.int/?mapFilter=vaccinations (accessed 2022-10-03).
- (4) Fontanet, A.; Autran, B.; Lina, B.; Kieny, M. P.; Karim, S. S. A.; Sridhar, D. SARS-CoV-2 variants and ending the COVID-19 pandemic. *Lancet* **2021**, *397*, 952–954.
- (5) Hall, L. R.; Sanchez, K.; da Graca, B.; Bennett, M. M.; Powers, M.; Warren, A. M. Income Differences and COVID-19: Impact on Daily Life and Mental Health. *Popul. Health Manag.* **2022**, 25, 384–391.
- (6) Merkoçi, A.; Li, C. Z.; Lechuga, L. M.; Ozcan, A. COVID-19 biosensing technologies. *Biosens. Bioelectron.* **2021**, *178*, 113046.

- (7) CDC 2019-Novel Coronavirus (2019-nCoV) Real-Time RT-PCR Diagnostic Panel. 2020. https://www.fda.gov/media/134922/download (accessed 2022-10-03).
- (8) Morales-Narváez, E.; Dincer, C. The impact of biosensing in a pandemic outbreak: COVID-19. *Biosens. Bioelectron.* **2020**, *163*, 112274.
- (9) Ogawa, T.; Fukumori, T.; Nishihara, Y.; Sekine, T.; Okuda, N.; Nishimura, T.; Fujikura, H.; Hirai, N.; Imakita, N.; Kasahara, K. Another false-positive problem for a SARS-CoV-2 antigen test in Japan. J. Clin. Virol. 2020, 131, 104612.
- (10) Liu, G.; Rusling, J. F. COVID-19 Antibody Tests and Their Limitations. ACS Sens. 2021, 6, 593-612.
- (11) Fathi-Hafshejani, P.; Azam, N.; Wang, L.; Kuroda, M. A.; Hamilton, M. C.; Hasim, S.; Mahjouri-Samani, M. Two-Dimensional-Material-Based Field-Effect Transistor Biosensor for Detecting COVID-19 Virus (SARS-CoV-2). ACS Nano 2021, 15, 11461–11469.
- (12) Wasfi, A.; Awwad, F.; Qamhieh, N.; Al Murshidi, B.; Palakkott, A. R.; Gelovani, J. G. Real-time COVID-19 detection via graphite oxide-based field-effect transistor biosensors decorated with Pt/Pd nanoparticles. *Sci. Rep.* **2022**, *12*, 18155.
- (13) Udugama, B.; Kadhiresan, P.; Kozlowski, H. N.; Malekjahani, A.; Osborne, M.; Li, V. Y. C.; Chen, H.; Mubareka, S.; Gubbay, J. B.; Chan, W. C. W. Diagnosing COVID-19: The Disease and Tools for Detection. *ACS Nano* **2020**, *14*, 3822–3835.
- (14) Seo, G.; Lee, G.; Kim, M. J.; Baek, S.-H.; Choi, M.; Ku, K. B.; Lee, C.-S.; Jun, S.; Park, D.; Kim, H. G.; et al. Rapid Detection of COVID-19 Causative Virus (SARS-CoV-2) in Human Nasopharyngeal Swab Specimens Using Field-Effect Transistor-Based Biosensor. ACS Nano 2020, 14, 5135–5142.
- (15) Cui, F.; Zhou, H. S. Diagnostic methods and potential portable biosensors for coronavirus disease 2019. *Biosens. Bioelectron.* **2020**, 165, 112349.
- (16) Shan, B.; Broza, Y. Y.; Li, W.; Wang, Y.; Wu, S.; Liu, Z.; Wang, J.; Gui, S.; Wang, L.; Zhang, Z.; et al. Multiplexed Nanomaterial-Based Sensor Array for Detection of COVID-19 in Exhaled Breath. *ACS Nano* **2020**, *14*, 12125–12132.
- (17) Poghossian, A.; Jablonski, M.; Molinnus, D.; Wege, C.; Schöning, M. J. Field-Effect Sensors for Virus Detection: From Ebola to SARS-CoV-2 and Plant Viral Enhancers. *Front. Plant Sci.* **2020**, *11*, 598103.
- (18) Sulleiro, M. V.; Dominguez-Alfaro, A.; Alegret, N.; Silvestri, A.; Gómez, I. J. 2D Materials towards sensing technology: From fundamentals to applications. *Sens. Bio-Sens. Res.* **2022**, *38*, 100540.
- (19) Hou, H.-L.; Anichini, C.; Samorì, P.; Criado, A.; Prato, M. 2D Van der Waals Heterostructures for Chemical Sensing. *Adv. Funct. Mater.* **2022**, 32, 2207065.
- (20) Ghaemi, F.; Amiri, A.; Bajuri, M. Y.; Yuhana, N. Y.; Ferrara, M. Role of different types of nanomaterials against diagnosis, prevention and therapy of COVID-19. *Sustain. Cities Soc.* **2021**, *72*, 103046.
- (21) Srivastava, A. K.; Dwivedi, N.; Dhand, C.; Khan, R.; Sathish, N.; Gupta, M. K.; Kumar, R.; Kumar, S. Potential of graphene-based materials to combat COVID-19: properties, perspectives, and prospects. *Mater. Today Chem.* **2020**, *18*, 100385.
- (22) Jabari, E.; Ahmed, F.; Liravi, F.; Secor, E. B.; Lin, L.; Toyserkani, E. 2D printing of graphene: a review. 2D Mater. 2019, 6, 042004.
- (23) Pola, C. C.; Rangnekar, S. V.; Sheets, R.; Szydlowska, B. M.; Downing, J. R.; Parate, K. W.; Wallace, S. G.; Tsai, D.; Hersam, M. C.; Gomes, C. L.; et al. Aerosol-jet-printed graphene electrochemical immunosensors for rapid and label-free detection of SARS-CoV-2 in saliva. 2d Mater. 2022, 9, 035016.
- (24) Jeong, J. H.; Kang, S.; Kim, N.; Joshi, R.; Lee, G.-H. Recent trends in covalent functionalization of 2D materials. *Phys. Chem. Chem. Phys.* **2022**, 24, 10684–10711.
- (25) Zhang, Y.; Zhu, Y.; Zheng, S.; Zhang, L.; Shi, X.; He, J.; Chou, X.; Wu, Z.-S. Ink formulation, scalable applications and challenging perspectives of screen printing for emerging printed microelectronics. *J. Energy Chem.* **2021**, *63*, 498–513.

- (26) Ali, M. A.; Hu, C.; Jahan, S.; Yuan, B.; Saleh, M. S.; Ju, E.; Gao, S.-J.; Panat, R. Sensing of COVID-19 Antibodies in Seconds via Aerosol Jet Nanoprinted Reduced-Graphene-Oxide-Coated 3D Electrodes. *Adv. Mater.* **2021**, 33, 2006647.
- (27) Suresh, R. R.; Lakshmanakumar, M.; Arockia Jayalatha, J. B. B.; Rajan, K. S.; Sethuraman, S.; Krishnan, U. M.; Rayappan, J. B. B. Fabrication of screen-printed electrodes: opportunities and challenges. *J. Mater. Sci.* **2021**, *56*, 8951–9006.
- (28) Jakus, A. E.; Secor, E. B.; Rutz, A. L.; Jordan, S. W.; Hersam, M. C.; Shah, R. N. Three-Dimensional Printing of High-Content Graphene Scaffolds for Electronic and Biomedical Applications. *ACS Nano* **2015**, *9*, 4636–4648.
- (29) Choong, Y. Y. C.; Tan, H. W.; Patel, D. C.; Choong, W. T. N.; Chen, C.-H.; Low, H. Y.; Tan, M. J.; Patel, C. D.; Chua, C. K. The global rise of 3D printing during the COVID-19 pandemic. *Nat. Rev. Mater.* **2020**, *5*, 637–639.
- (30) Crevillen, A. G.; Mayorga-Martinez, C. C.; Vaghasiya, J. V.; Pumera, M. 3D-Printed SARS-CoV-2 RNA Genosensing Microfluidic System. *Adv. Mater. Technol.* **2022**, *7*, 2101121.
- (31) Wang, J.; Xu, Z.; Zhang, M.; Liu, J.; Zou, H.; Wang, L. Improvement of electrochemical performance of screen-printed carbon electrodes by UV/ozone modification. *Talanta* **2019**, *192*, 40–45.
- (32) Sundeep, D.; Varadharaj, E. K.; Umadevi, K.; Jhansi, R. Review—Role of Nanomaterials in Screenprinted Electrochemical Biosensors for Detection of Covid-19 and for Post-Covid Syndromes. *ECS Adv.* **2023**, *2*, 016502.
- (33) Szydlowska, B. M.; Cai, Z.; Hersam, M. C. Printed nanomaterial sensor platforms for COVID-19 and future pandemics. *Curr. Opin. Solid State Mater. Sci.* **2023**, 27, 101121.
- (34) Rahmati, Z.; Roushani, M.; Hosseini, H.; Choobin, H. Electrochemical immunosensor with Cu(2)O nanocube coating for detection of SARS-CoV-2 spike protein. *Mikrochim. Acta* **2021**, *188*, 1–9
- (35) Drobysh, M.; Liustrovaite, V.; Baradoke, A.; Viter, R.; Chen, C.-F.; Ramanavicius, A.; Ramanaviciene, A. Determination of rSpike Protein by Specific Antibodies with Screen-Printed Carbon Electrode Modified by Electrodeposited Gold Nanostructures. *Biosensors* **2022**, *12*, 593.
- (36) Drobysh, M.; Ramanavicius, A.; Baradoke, A. Polyaniline-based electrochemical immunosensor for the determination of antibodies against SARS-CoV-2 spike protein. *Sci. Total Environ.* **2023**, *862*, 160700.
- (37) Ratautaite, V.; Boguzaite, R.; Brazys, E.; Ramanaviciene, A.; Ciplys, E.; Juozapaitis, M.; Slibinskas, R.; Bechelany, M.; Ramanavicius, A. Molecularly imprinted polypyrrole based sensor for the detection of SARS-CoV-2 spike glycoprotein. *Electrochim. Acta* 2022, 403, 139581.
- (38) Hatamluyi, B.; Rezayi, M.; Amel Jamehdar, S.; Rizi, K. S.; Mojarrad, M.; Meshkat, Z.; Choobin, H.; Soleimanpour, S.; Boroushaki, M. T. Sensitive and specific clinically diagnosis of SARS-CoV-2 employing a novel biosensor based on boron nitride quantum dots/flower-like gold nanostructures signal amplification. *Biosens. Bioelectron.* 2022, 207, 114209.
- (39) Amouzadeh Tabrizi, M.; Acedo, P. Highly Sensitive RNA-Based Electrochemical Aptasensor for the Determination of C-Reactive Protein Using Carbon Nanofiber-Chitosan Modified Screen-Printed Electrode. *Nanomater.* 2022, 12, 415.
- (40) Wu, L.; Wang, X.; Wu, C.; Cao, X.; Tang, T.; Huang, H.; Huang, X. Ultrasensitive SARS-CoV-2 diagnosis by CRISPR-based screen-printed carbon electrode. *Anal. Chim. Acta* **2022**, *1221*, 340120.
- (41) Stefano, J. S.; Guterres e Silva, L. R.; Rocha, R. G.; Brazaca, L. C.; Richter, E. M.; Abarza Muñoz, R. A.; Janegitz, B. C. New conductive filament ready-to-use for 3D-printing electrochemical (bio)sensors: Towards the detection of SARS-CoV-2. *Anal. Chim. Acta* 2022, 1191, 339372.
- (42) de Moraes, A. C. M.; Obrzut, J.; Sangwan, V. K.; Downing, J. R.; Chaney, L. E.; Patel, D. K.; Elmquist, R. E.; Hersam, M. C.

- Elucidating charge transport mechanisms in cellulose-stabilized graphene inks. J. Mater. Chem. C 2020, 8, 15086–15091.
- (43) He, P.; Cao, J.; Ding, H.; Liu, C.; Neilson, J.; Li, Z.; Kinloch, I. A.; Derby, B. Screen-Printing of a Highly Conductive Graphene Ink for Flexible Printed Electronics. ACS Appl. Mater. Interfaces 2019, 11, 32225–32234.
- (44) García-Miranda Ferrari, A.; Rowley-Neale, S. J.; Banks, C. E. Screen-printed electrodes: Transitioning the laboratory in-to-the field. *Talanta Open* **2021**, *3*, 100032.
- (45) Wang, J. Analytical Electrochemistry; John Wiley & Sons: 2023.
- (46) Elgrishi, N.; Rountree, K. J.; McCarthy, B. D.; Rountree, E. S.; Eisenhart, T. T.; Dempsey, J. L. A Practical Beginner's Guide to Cyclic Voltammetry. *J. Chem. Educ.* **2018**, *95*, 197–206.
- (47) Magar, H. S.; Hassan, R. Y. A.; Mulchandani, A. Electrochemical Impedance Spectroscopy (EIS): Principles, Construction, and Biosensing Applications. *Sensors* **2021**, *21*, 6578.
- (48) Macwan, I.; Khan, M. D. H.; Aphale, A.; Singh, S.; Liu, J.; Hingorani, M.; Patra, P. Interactions between avidin and graphene for development of a biosensing platform. *Biosens. Bioelectron.* **2017**, *89*, 326–333.
- (49) Lazanas, A. C.; Prodromidis, M. I. Electrochemical Impedance Spectroscopy A Tutorial. ACS Meas. Sci. Au 2023, 3, 162.
- (50) Nicholson, R. S. Theory and Application of Cyclic Voltammetry for Measurement of Electrode Reaction Kinetics. *Anal. Chem.* **1965**, *37*, 1351–1355.
- (51) Secor, E. B.; Gao, T. Z.; Islam, A. E.; Rao, R.; Wallace, S. G.; Zhu, J.; Putz, K. W.; Maruyama, B.; Hersam, M. C. Enhanced Conductivity, Adhesion, and Environmental Stability of Printed Graphene Inks with Nitrocellulose. *Chem. Mater.* **2017**, *29*, 2332–2340.
- (52) Parate, K.; Pola, C. C.; Rangnekar, S. V.; Mendivelso-Perez, D. L.; Smith, E. A.; Hersam, M. C.; Gomes, C. L.; Claussen, J. C. Aerosol-jet-printed graphene electrochemical histamine sensors for food safety monitoring. 2D Mat 2020, 7 (3), 034002.
- (53) Barsoukov, E.; Macdonald, J. R. Impedance Spectroscopy: Theory, Experiment, and Applications; Wiley: 2005.
- (54) Randviir, E. P.; Banks, C. E. Electrochemical impedance spectroscopy: an overview of bioanalytical applications. *Anal. Methods* **2013**, *5*, 1098–1115.
- (55) Magar, H. S.; Hassan, R. Y. A.; Mulchandani, A. Electrochemical Impedance Spectroscopy (EIS): Principles, Construction, and Biosensing Applications. *Sensors* **2021**, *21*, 6578.
- (56) Bard, A. J.; Faulkner, L. R. Electrochemical Methods: Fundamentals and Applications, 2nd ed.; John Wiley & Sons, Inc.:
- (57) Muhammad, H.; Tahiri, I. A.; Muhammad, M.; Masood, Z.; Versiani, M. A.; Khaliq, O.; Latif, M.; Hanif, M. A comprehensive heterogeneous electron transfer rate constant evaluation of dissolved oxygen in DMSO at glassy carbon electrode measured by different electrochemical methods. *J. Electroanal. Chem.* **2016**, *775*, 157–162.
- (58) Torres, M. D. T.; de Araujo, W. R.; de Lima, L. F.; Ferreira, A. L.; de la Fuente-Nunez, C. Low-cost biosensor for rapid detection of SARS-CoV-2 at the point of care. *Matter* **2021**, *4*, 2403–2416.
- (59) Malla, P.; Liao, H.-P.; Liu, C.-H.; Wu, W.-C.; Sreearunothai, P. Voltammetric biosensor for coronavirus spike protein using magnetic bead and screen-printed electrode for point-of-care diagnostics. *Mikrochim. Acta* **2022**, *189*, 168.
- (60) Fabiani, L.; Saroglia, M.; Galatà, G.; De Santis, R.; Fillo, S.; Luca, V.; Faggioni, G.; D'Amore, N.; Regalbuto, E.; Salvatori, P.; et al. Magnetic beads combined with carbon black-based screen-printed electrodes for COVID-19: A reliable and miniaturized electrochemical immunosensor for SARS-CoV-2 detection in saliva. *Biosens. Bioelectron.* **2021**, *171*, 112686.
- (61) Mehmandoust, M.; Gumus, Z. P.; Soylak, M.; Erk, N. Electrochemical immunosensor for rapid and highly sensitive detection of SARS-CoV-2 antigen in the nasal sample. *Talanta* **2022**, 240, 123211.
- (62) Fortunati, S.; Giliberti, C.; Giannetto, M.; Bolchi, A.; Ferrari, D.; Donofrio, G.; Bianchi, V.; Boni, A.; De Munari, I.; Careri, M.

- Rapid Quantification of SARS-Cov-2 Spike Protein Enhanced with a Machine Learning Technique Integrated in a Smart and Portable Immunosensor. *Biosensors* **2022**, *12*, 426.
- (63) Hussein, H. A.; Kandeil, A.; Gomaa, M.; Mohamed El Nashar, R.; El-Sherbiny, I. M.; Hassan, R. Y. A. SARS-CoV-2-Impedimetric Biosensor: Virus-Imprinted Chips for Early and Rapid Diagnosis. *ACS Sens.* **2021**, *6*, 4098–4107.
- (64) WHO. COVID-19 Target product profiles for priority diagnostics to support response to the COVID-19 Pandemic v.1.0. World Health Organization. R&D Blueprint, 2020.
- (65) Perchetti, G. A.; Huang, M. L.; Mills, M. G.; Jerome, K. R.; Greninger, A. L. Analytical Sensitivity of the Abbott BinaxNOW COVID-19 Ag Card. J. Clin. Microbiol. 2021, 59, 10–1128.
- (66) Deeks, J. J.; Singanayagam, A.; Houston, H.; Sitch, A. J.; Hakki, S.; Dunning, J.; Lalvani, A. SARS-CoV-2 antigen lateral flow tests for detecting infectious people: linked data analysis. *BMJ* **2022**, *376*, e066871.
- (67) Joshua, M. D.; Thomas, T.; Mitch, B.; Yano, Y.; Julian, D.; Charlene, M.; George, T.; Mona, T.; Socheata, C.; Bowen, Z.; et al. Assessment of twenty-two SARS-CoV-2 rapid antigen tests against SARS-CoV-2: A laboratory evaluation study. *MedRxiv* 2021, 2021–12.
- (68) Stanley, S.; Hamel, D. J.; Wolf, I. D.; Riedel, S.; Dutta, S.; Contreras, E.; Callahan, C. J.; Cheng, A.; Arnaout, R.; Kirby, J. E.; Kanki, P. J.; et al. Limit of Detection for Rapid Antigen Testing of the SARS-CoV-2 Omicron and Delta Variants of Concern Using Live-Virus Culture. *J. Clinic. Microbiol.* **2022**, *60*, e00140–00122.
- (69) CDC. CDC 2019-Novel Coronavirus (2019-nCoV) Real-Time RT-PCR Diagnostic Panel. 2023, CDC-006-00019.
- (70) Ham, R. E.; Smothers, A. R.; King, K. L.; Napolitano, J. M.; Swann, T. J.; Pekarek, L. G.; Blenner, M. A.; Dean, D. Efficient SARS-CoV-2 Quantitative Reverse Transcriptase PCR Saliva Diagnostic Strategy utilizing Open-Source Pipetting Robots. *JoVE* **2022**, *180*, e63395.
- (71) Rennert, L.; McMahan, C.; Kalbaugh, C. A.; Yang, Y.; Lumsden, B.; Dean, D.; Pekarek, L.; Colenda, C. C. Surveillance-based informative testing for detection and containment of SARS-CoV-2 outbreaks on a public university campus: an observational and modeling study. *Lancet Child Adolesc. Health* **2021**, *5*, 428–436.
- (72) McMahan, C. S.; Lewis, D.; Deaver, J. A.; Dean, D.; Rennert, L.; Kalbaugh, C. A.; Shi, L.; Kriebel, D.; Graves, D.; Popat, S. C.; et al. Predicting COVID-19 Infected Individuals in a Defined Population from Wastewater RNA Data. ACS ES&T Water 2022, 2, 2225–2232.
- (73) Ham, R. E.; Smothers, A. R.; Che, R.; Sell, K. J.; Peng, C. A.; Dean, D. Identifying SARS-CoV-2 Variants of Concern through Saliva-Based RT-qPCR by Targeting Recurrent Mutation Sites. *Microbiol. Spectr.* **2022**, *10*, e0079722.
- (74) Plumb, E. V.; Ham, R. E.; Napolitano, J. M.; King, K. L.; Swann, T. J.; Kalbaugh, C. A.; Rennert, L.; Dean, D. Implementation of a Rural Community Diagnostic Testing Strategy for SARS-CoV-2 in Upstate South Carolina. *Front. Public Health* **2022**, *10*, 858421.
- (75) McNaught, A. D.; Wilkinson, A. *IUPAC Compendium of Chemical Terminology*; Blackwell Scientific Publications: 1997.